

# Accuracy and precision of laser spectrometers for trace gas sensing in the presence of optical fringes and atmospheric turbulence

P. Werle

Received: 22 March 2010 / Revised version: 2 July 2010 / Published online: 8 August 2010  
© Springer-Verlag 2010

**Abstract** Spectroscopic techniques are increasingly used for field laser applications in industry and research. Under field conditions complex gas sensors cannot be considered as stable and therefore drift characterization is a key issue to distinguish between sample data and sensor drift. In this paper the history of von Neumann's two-sample variance and Allan variance stability investigations in the field of frequency metrology and the relationship to wavelet analysis are reviewed. The concept has been used to characterize accuracy and precision of spectroscopic data in the time domain and practical guidelines for the interpretation of  $\sigma/\tau$  plots are presented. Two topics relevant for spectroscopic measurements are discussed: First, the optical fringe effect, which is present in any spectrometer, limits the precision and accuracy of spectroscopic measurements by forming time dependent background structures superimposed to the signal under investigation. The two-sample variance is used to characterize optical etalons and long-term drift using  $\sigma/\tau$  plots. Second, the short-term instrument stability characteristic in the presence of atmospheric turbulence is discussed. This is important for laser-based gas monitors measuring the turbulent transport of trace gases between the biosphere and the atmosphere using the eddy-covariance technique. It will be shown how the spectral characteristics of turbulence in the Kolmogorov inertial subrange can be identified in the time domain and how the effect of optical fringes can be separated from atmospheric signals.

## 1 Introduction

Modern spectroscopic techniques based on semiconductor lasers are increasingly used for field laser applications in industry and research [1–8]. Under field conditions these complex measurement devices cannot be considered as stable and drift characterization is still a key issue to distinguish between sample data and sensor drift. The question is how drift in such instruments can influence precision and accuracy of the measurement. In 1816 Gauss [9] described the distribution of observation to be normal with a probability density function (PDF) proportional to  $h \cdot \exp(-h^2 x^2)$ . He named the positive constant  $h$  the precision, which later was replaced by the standard deviation  $\sigma = 1/\sqrt{2}h$ . In general, precision and accuracy describe the relationship between a measured value and the true value. To investigate precision and accuracy a series of successive measurements of a known concentration have to be recorded. When these data are then plotted as a frequency distribution it is expected from the central limit theorem, that the acquired data are normally distributed [10]. The mean occurs at the center of the distribution, and represents the best estimate based on all of the measured data. The standard deviation describes the width of the distribution as the variation that occurs between successive measurements. The amount of shift from the true value is called the accuracy of the measurement. The width of the distribution indicates that individual measurements may not agree well with each other. This precision of the measurement is expressed by quoting the standard deviation. In cases where a measurement that has a high accuracy, but a low precision, the histogram is centered over the true value, but the distribution is very broad. Although the measurements are correct as a group, each individual reading is a poor measure of the true value. Poor precision results from random noise or errors, which change each time the measurement is repeated and averaging several measurements

---

P. Werle (✉)  
Karlsruhe Institute of Technology KIT, Institute of Meteorology  
and Climate Research IMK-IFU, Kreuzeckbahnstrasse 19, 82467  
Garmisch-Partenkirchen, Germany  
e-mail: [Peter.Werle@kit.edu](mailto:Peter.Werle@kit.edu)  
Fax: +49-08821-73573

will improve the precision. In cases where a measurement is very precise but has poor accuracy this makes the distribution very narrow, but not centered over the true value. Poor accuracy results from systematic errors repeated in the same manner each time the measurement is conducted. Accuracy usually depends on system calibration and averaging of individual measurements does not improve the accuracy. Precision is a measure of noise and accuracy is a measure of calibration. In practice, averaging of successive data should improve the measurement quality and we call it precision, otherwise we have to deal with accuracy, where calibration should correct the error. This requires some thought on how the system has to be calibrated, and how often it should be done [11].

Historically, the question of drift came up for practical applications in ballistic research, where it is almost impossible because of atmospheric conditions to get two successive observations under exactly the same conditions for the calculation of range tables and, therefore, it is necessary to know the variance amongst a group of projectiles fired under exactly similar conditions [12]. Already in 1941 John von Neumann et al. [13] mentioned that *‘there are cases, where the standard deviation may be held constant, but the mean varies from one observation to the next. If no correction is made for such a variation of the mean and the standard deviation is computed from the data in the conventional way, then the estimated standard deviation value will tend to be larger than the true population value. When the variation in the mean is gradual, so that a trend, which need not be linear, is shifting the mean, a rather simple method of minimizing the effect of the trend on dispersion is to estimate standard deviation from differences’*. Therefore, von Neumann proposed a variance based upon mean square successive differences as

$$\delta^2 = \frac{1}{n-1} \sum_{i=1}^{n-1} (y_{i+1} - y_i)^2. \quad (1)$$

The subscript  $i$  in this expression refers to the temporal order of the observation  $y_i$ . Von Neumann proposed to use  $\delta^2$  to estimate standard deviation (where it is implicitly assumed that the  $y_i$  are random and uncorrelated) and to determine whether a trend actually exists. The two-sample variance  $\delta^2$  measures the variance independently of the order of observations and therefore includes the effect of any drift. Von Neumann has shown that the expectation value of  $\delta^2$  from random samples is  $2\sigma^2$  and since then the *‘half’ mean square successive difference* in the notation of Hald [14–16] has been investigated. In 1964 a subcommittee on frequency stability was formed within the Institute of Electrical and Electronic Engineers (IEEE) standards committee to propose definitions for measures on frequency and phase stabilities, which is of importance to characterize and specify

oscillators for frequency and time standards. It has been analyzed what happens to the standard deviation when the data set may be characterized by power-law spectra which are more dispersive than classical white noise frequency fluctuations [17]. Fluctuations characterized by flicker noise or any other pink noise can be considered as drift and have an impact on the standard deviation in a similar way as atmospheric conditions in ballistic research. For example, using  $1/f$  noise as a model, as the number of data points increases, the standard deviation monotonically increases without limit. For measurements of frequency stability the two-sample frequency variance is known as the ‘Allan variance’ [18, 19] and an experimental estimation of this measure is

$$\sigma_y^2(\tau) \equiv \frac{1}{2} \langle (\bar{y}_{k+1} - \bar{y}_k)^2 \rangle \quad \text{with} \quad \bar{y}_k(\tau) = \frac{1}{\tau} \cdot \int_{t_k}^{t_k+\tau} y(t) dt \quad (2)$$

where  $t_{k+1} = t_k + \tau$ , and  $k$  and  $k + 1$  are adjacent samples and  $\langle \rangle$  is the expectation value. This equation is easy to implement experimentally as one simply needs to add up the squares of the differences between adjacent averaged  $\bar{y}_k(\tau)$  over intervals  $\tau$ , divide by the number of them and by two, and take the square root. The IEEE has recommended this quantity for specification of stability of time and frequency standards in the time domain denoted by  $\sigma_y(\tau)$ . This measure of stability in frequency generators has gained general acceptance among users of frequency and time standards [20]. The concept of the two-sample variance has been applied in high speed communication systems to estimate the clock drift in computer clusters [21], in astronomy to evaluate the radiometer stability [22, 23], to characterize nanovoltmeters [24], to describe earth rotation variations that are derived from the different geodetic techniques like laser ranging to artificial satellites [25] and there are requirements for medical applications [26].

In 1993 Werle et al. [27] applied the concept of the Allan variance to characterize the signal drift in a tunable diode-laser spectrometer and since then this method became widely accepted in the diode-laser spectroscopy community. Researchers and manufacturers apply the concept to demonstrate the performance of their instruments. Approaches to improve sensitivity of spectrometers by double modulation techniques using Kerr rotation [28], Stark modulation [29], Faraday modulation [30], sub-Doppler NICE-OHMS [31], photo-acoustic spectroscopy (PAS) [32], cantilever enhanced PAS [33] or quartz tuning fork enhanced PAS [34] have been characterized this way. Stability investigations have been reported in stable isotope ratio infrared spectroscopy [35] for carbon dioxide [36–41], water vapor [42–45], methane [46] and for nitrous oxide [47]. It

has also been applied to medical and air quality measurements [48, 49]. Airborne [50–52] and ground-based [53–65] atmospheric research identifies new measurement challenges. Such a challenge is the trace gas exchange between the biosphere and the atmosphere and meanwhile in the field of ecosystem research the two-sample variance is frequently applied to validate the performance of the measurement system [66–74]. During spectroscopic measurement applications both, accuracy and precision are generally affected by white noise and noise contributions with power-law spectra and time dependent background structures. While these have been discussed previously [27] this paper focuses on two key issues in the context of spectroscopic measurements: The first is the etalon effect, which can be observed in most spectrometers and limits the performance due to the presence of time dependent background structures. An analysis based on a two-sample variance can be used to identify and to characterize these optical fringes and any long-term drift. The second topic deals with time resolution requirements for measurements of atmospheric turbulent transport. It will be shown how, in analogy to the Fourier domain, atmospheric turbulence can be characterized in the time domain. This is of importance for trace gas flux measurement applications, where it must be ensured that all contributions in the turbulence spectrum to the vertical transport are included in the measurement. Furthermore predictions about accuracy and precision of the instrument can be made as a function of integration time and several examples of ‘Sigma/Tau’, ‘ $\sigma/\tau$ ’ or ‘Allan’ plots will be discussed.

## 2 Estimates of the two-sample variance

The stability of a measurement system can be characterized either by variances averaged during a given time interval  $\tau$  in the time domain or by the power spectral density of time series data, which is the energy distribution in the Fourier frequency spectrum. The power spectral density (PSD) is important because it carries more information than the time-domain variance and therefore provides unambiguous identification of the noise process encountered in the system under investigation. Time-domain and frequency-domain parameters naturally are not independent and the true variance  $\sigma^2$  of a stationary zero-mean continuous time signal  $y(t)$  is defined as the time-average of the product  $y(t) \cdot y(t + \Delta t)$  through the autocorrelation function

$$R_y(\Delta t) = \langle y(t) \cdot y(t + \Delta t) \rangle \quad (3)$$

where  $\langle \rangle$  is the mathematical expectation operator [75]. Historically the single-sided PSD  $S_y(f)$  has been utilized to define the variance for zero lag  $\Delta t = 0$  as

$$\sigma^2 = R_y(0) = \int_0^\infty S_y(f) df \quad (4)$$

For time series signals with a power-law spectrum, the PSD can be expressed as  $S_y(f) = h_\alpha f^\alpha$  and for integer values  $\alpha < 0$ ,  $f^\alpha$  diverges for  $f$  approaching zero and then the integral (4) is infinite. When analyzing variances to characterize the stability of spectroscopic instrumentation the long-term behavior is determined by the components of the PSD at low frequencies, when  $f$  tends towards zero. Therefore we average the time series signal  $y(t)$  for a time  $\tau$  and analyze the variance of the averaged signal  $\bar{y}(t, \tau)$ .

$$\bar{y}(t, \tau) = \frac{1}{\tau} \int_t^{t+\tau} y(t) dt \quad (5)$$

The time series  $\bar{y}(t, \tau)$  is the output of a moving average filter of length  $\tau$  with an impulse response  $a(t, \tau)$  defined by

$$a(t, \tau) = \frac{1}{\tau} \text{rect}(t) = \begin{cases} \frac{1}{\tau} & \text{for } 0 \leq t \leq \tau \\ 0 & \text{elsewhere} \end{cases} \quad (6)$$

which is a rectangular window of width  $\tau$  and height  $1/\tau$  (Fig. 1a). Thus, in the time domain,  $\bar{y}(t, \tau)$  is defined as the convolution (denoted by the asterisk  $*$ )

$$\bar{y}(t, \tau) = a(t, \tau) * y(t) \quad (7)$$

The Fourier transform of the convolving function  $a(t, \tau)$  provides the frequency response  $A(f)$  of the moving average filter as

$$A(f) = \int_{-\infty}^{+\infty} a(t, \tau) \cdot e^{-i2\pi ft} dt = \frac{\sin(\pi f \tau)}{\pi f \tau} \cdot e^{i\pi f \tau} \quad (8)$$

The PSD  $S_{\bar{y}}(f)$  of the time series  $\bar{y}(t, \tau)$  is  $S_{\bar{y}}(f) = L(f) \cdot S_y(f)$ , where the squared modulus of the Fourier transform  $L(f) = |A(f)|^2$  is the transfer function (Fig. 1b) of the moving average filter

$$L(f) = \frac{\sin^2(\pi f \tau)}{(\pi f \tau)^2} \quad (9)$$

From (4) and (9) the variance of the averaged signal  $\bar{y}(t, \tau)$  is expressed by:

$$\sigma_{\bar{y}}^2(\tau) = \int_0^\infty L(f) \cdot S_y(f) df \quad (10)$$

For power-law spectra  $S_y(f) = h_\alpha f^\alpha$  with  $\alpha < 0$ , the variance  $\sigma_{\bar{y}}^2(\tau)$  is not defined because the low-pass filter  $L(f)$  is unity for  $f \rightarrow 0$ . For the variance  $\sigma_{\bar{y}}^2(\tau)$  to be defined for  $\alpha < 0$  an additional filter  $H(f)$  has to be applied in series with  $L(f)$ . If the filter  $H(f)$  acts on the previously low-pass filtered signal  $\bar{y}(t, \tau)$  to provide the output signal  $\Delta \bar{y}(t, \tau)$ , its variance  $\sigma_{\Delta \bar{y}}^2(\tau)$  can be written for the power-law spectrum as

$$\sigma_{\Delta \bar{y}}^2(\tau) = \int_0^\infty H(f) \cdot \frac{\sin^2(\pi f \tau)}{(\pi f \tau)^2} \cdot h_\alpha f^\alpha df \quad (11)$$

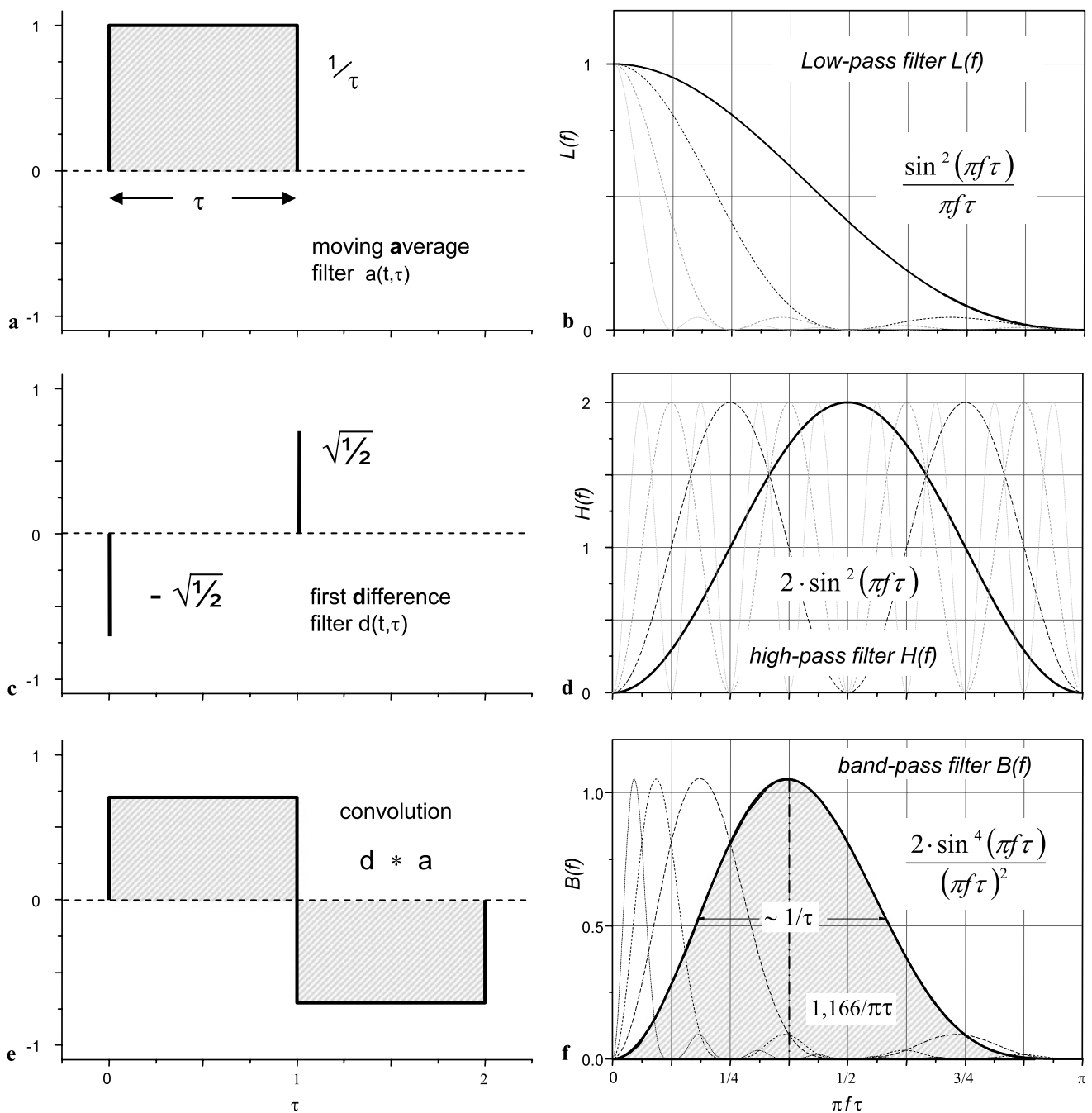


**Fig. 1** The moving average filter (a) is a low-pass with a sinc transfer function (b). The normalized first difference filter (c) represents a high-pass filter (d). The convolution of both filters (e) forms a constant Q band-pass filter (f)

A derivation in the time domain is equivalent to a multiplication by  $f^2$  in the PSD domain and a filter with a frequency response  $D(f) \sim f^\mu$  can be obtained by applying  $\mu$  time derivations to the signal  $\bar{y}(t, \tau)$ . The variance  $\sigma_{\Delta\bar{y}}^2(\tau)$  is defined if  $f^\alpha \cdot H(f)$  converges for  $f \rightarrow 0$ , which requires that the transfer function  $H(f) = |D(f)|^2 \sim f^{2\mu}$  with  $\mu > -\alpha/2$  when  $f$  approaching zero and for  $\mu = 1$  the variance  $\sigma_{\Delta\bar{y}}^2(\tau)$  is defined for  $\alpha > -2$ . A basic approxima-

tion for a derivation is a first order difference filter, which substitutes the value of every data point of a time series by the difference of two subsequent points [76]. Then the required impulse response of the filtered data set (Fig. 1c) is

$$d(t, \tau) = \begin{cases} +\frac{1}{\sqrt{2}} & t = \tau \\ -\frac{1}{\sqrt{2}} & t = 0 \\ 0 & \text{elsewhere} \end{cases} \quad (12)$$

The purpose of this filter is twofold and it should assure convergence for the variance, but also the filter should not modify white noise. Therefore, it is normalized  $\|d^2(t, \tau)\| = 1$  and the Fourier transform of the first order difference filter is

$$D(f) = \int_{-\infty}^{+\infty} d(t, \tau) \cdot e^{-i2\pi ft} dt = \sqrt{2} \cdot \sin(\pi f \tau) \cdot e^{-i \frac{2\pi f \tau + \pi}{2}} \tag{13}$$

The transfer function  $H(f) = |D(f)|^2$  shows the effect of the filter on the amplitude of the power spectrum (Fig. 1d) and is given as

$$H(f) = 2 \cdot \sin^2(\pi f \tau) \tag{14}$$

At low frequencies the amplitude approaches zero and the filter acts like a high-pass one. This allows us to study the asymptotic behavior of  $S_y(f)$ , when  $f \rightarrow 0$  and therefore the approach is useful to study the asymptotic behavior of drift in time series signals. The convolution of the first order difference impulse response with the moving average filter leads to a new time series (Fig. 1e)

$$\Delta \bar{y}(t, \tau) = d(t, \tau) * [a(t, \tau) * y(t)] = d(t, \tau) * \bar{y}(t) = \frac{1}{\sqrt{2}} (\bar{y}(t + \tau) - \bar{y}(t)) \tag{15}$$

In terms of filtering, the two-sample variance can be interpreted as an analysis using a ‘constant  $Q$ ’ band-pass filter  $B(f) = L(f) \cdot H(f)$ , where the ratio of the pass-band center frequency and width is fixed (Fig. 1f). The peaks located at  $f = 1, 166/\pi \tau$  have an amplitude 1.05 independent of  $\tau$ , while the width of the peak is proportional to  $1/\tau$ . Peaks at higher frequencies are damped by  $1/f^2$ . The normalized variance of a band-pass filtered time series is then expressed in the frequency domain as

$$\sigma_{\Delta \bar{y}}^2(\tau) = \int_0^\infty \frac{2 \cdot \sin^4(\pi f \tau)}{(\pi f \tau)^2} S_y(f) df \tag{16}$$

This variance  $\sigma_{\Delta \bar{y}}^2(\tau)$  is the frequency-domain representation of the time-domain two-sample (Allan) variance  $\sigma_A^2(\tau)$

[17–20, 27], which has been introduced in (2). The definition of  $\Delta \bar{y}(t, \tau)$  leads to

$$\sigma_{\Delta \bar{y}}^2(\tau) = \langle \Delta \bar{y}^2(t, \tau) \rangle \stackrel{(15)}{=} \frac{1}{2} \langle (\bar{y}(t + \tau) - \bar{y}(t))^2 \rangle \stackrel{(2)}{=} \sigma_y^2(\tau) \tag{17}$$

The factor of 1/2 was introduced through (12) to normalize the two-sample variance to the variance of the mean in the limit of white noise ( $\alpha = 0$ ), where the mean  $\bar{y}(t) = \bar{y}(t + \tau) = 0$  and

$$\sigma_{\Delta \bar{y}}^2(\tau) = \frac{1}{2} (\langle \bar{y}^2(t + \tau) \rangle + \langle \bar{y}^2(t) \rangle - 2 \langle \bar{y}(t + \tau) \bar{y}(t) \rangle) = \langle \bar{y}^2(t) \rangle = \sigma_y^2 = \sigma^2/\tau \tag{18}$$

The two-sample (Allan) variance is defined for power-law spectra  $S_y(f) = h_\alpha f^\alpha$  with  $\alpha > -2$ . For positive  $\alpha$  values we must apply a high-frequency cut-off as the upper limit of the integral to assure the convergence. Evaluation of the integral definition (16) provides the information about the asymptotic behavior of the variance for the various noise types, and for time series data with a power-law spectrum analytic expressions have been derived. The asymptotic forms of  $\sigma_y^2(\tau)$  for power-law types relevant for spectroscopic applications [17–20] are listed in Table 1 and  $\alpha = 0$  is the case of *white noise*,  $\alpha = -1$  is called *flicker noise*,  $\alpha = -2$  corresponds to the *random walk*. For  $\alpha$  in the range  $-2 \leq \alpha < 1$  the two-sample variance is proportional to  $\tau^\mu$  where  $\mu = -\alpha - 1$ . A  $\sigma/\tau$  plot of the log of the two-sample variance as a function of the log of the averaging time  $\tau$  shows the asymptotic behavior of  $S_y(f)$ , when  $f$  approaches zero and therefore allows to characterize drift and noise in time series signals. Even though  $\sigma_y^2(\tau)$  will not be normally distributed, the variance of the average of  $M$  independent, non-overlapping samples of  $\sigma_y^2(\tau)$  will decrease as  $1/M$  provided the conditions on low-frequency divergence are met. For large  $M$ , the distribution of the  $m$  sample averages of  $\sigma_y^2(\tau)$  will tend toward a normal distribution according to the central limit theorem and confidence intervals based on the normal distribution can be estimated. There are several ways to define an estimator for the two-sample variance as a function of the averaging time  $\tau$ .

**Table 1** Asymptotic forms of  $\sigma_y^2(\tau)$  for various power-law types

	$S_y(f) = h_\alpha f^\alpha$		$\sigma_y^2(\tau) \approx  \tau ^\mu$
$\alpha = -2$	$S_y(f) = h_{-2} f^{-2}$	$\mu = 1$	$\sigma_y^2(\tau) = h_{-2} \frac{(2\pi)^2}{3} \cdot  \tau $
$\alpha = -1$	$S_y(f) = h_{-1} f^{-1}$	$\mu = 0$	$\sigma_y^2(\tau) = h_{-1} 2 \ln 2$
$\alpha = 0$	$S_y(f) = h_0 f^0$	$\mu = -1$	$\sigma_y^2(\tau) = \frac{1}{2} h_0 \cdot  \tau ^{-1}$
$\alpha = +1$	$S_y(f) = h_1 f^1$	$\mu = -2$	$\sigma_y^2(\tau) = \frac{1}{(2\pi)^2} h_1 \cdot \tau^{-2} [1.038 + 3 \ln(2\pi f_h \tau)]$
$\alpha = +2$	$S_y(f) = h_2 f^2$	$\mu = -2$	$\sigma_y^2(\tau) = \frac{1}{(2\pi)^2} h_2 \cdot 3 f_h \tau^{-2}$

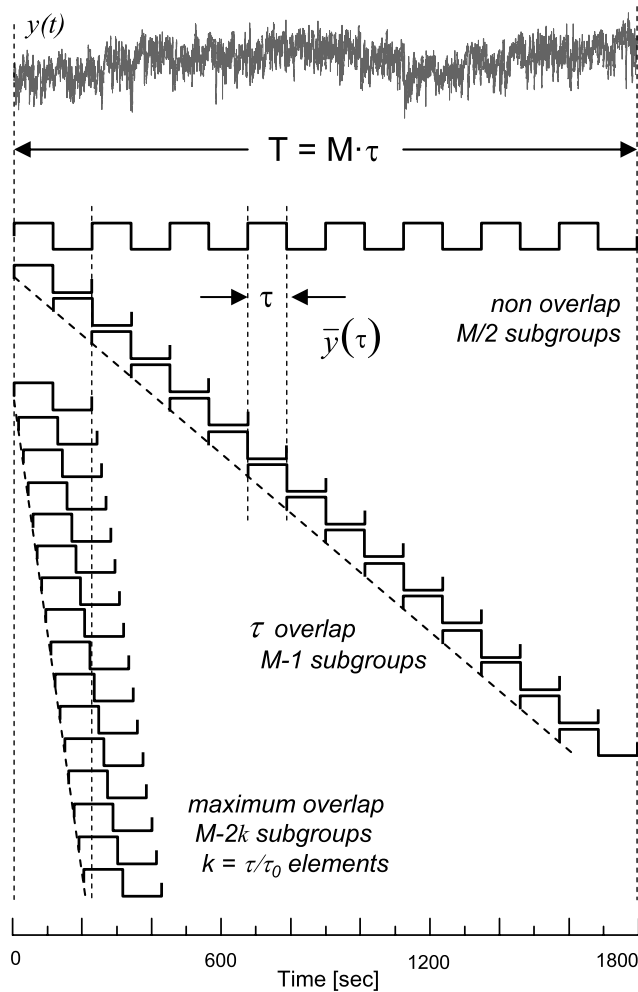


**Fig. 2** Estimates for the two-sample variance can be calculated from non-overlapping,  $\tau$ -overlap or maximum overlap subgroups of time series data

If we look at consecutive averages  $(\bar{y}_1, \bar{y}_2, \bar{y}_3, \bar{y}_4, \dots)$  we could calculate a two-sample variance from  $\bar{y}_1$  and  $\bar{y}_2$  as well as from  $\bar{y}_3$  and  $\bar{y}_4$ . The average of two variances provides an improved estimate of the true two-sample variance and we can expect a better confidence than for a single difference. For subgroups  $M = N/k = T/\tau$  with  $k$  elements each which are taken from  $N$  measurement during a time interval  $T$  as shown in Fig. 2, the ‘non-overlapping’ estimate  $(\bar{y}_1 - \bar{y}_2, \bar{y}_3 - \bar{y}_4, \dots, \bar{y}_{(N/2k)-1} - \bar{y}_{N/2k})$  uses  $M/2$  independent differences, while for a ‘ $\tau$ -overlap’ estimate  $(\bar{y}_1 - \bar{y}_2, \bar{y}_2 - \bar{y}_3, \dots, \bar{y}_{(N/k)-1} - \bar{y}_{N/k})$  subgroup averages are used twice and an improved estimate based upon  $M - 1$  differences is obtained. The most efficient use is to average all possible two-sample variances of a given  $\tau$ -subgroup. The ‘maximum overlap’ sample variance uses all  $N - 2k + 1$  successive differences and therefore provides the most efficient estimate, but a problem arises when estimating the confidence intervals and the number of degrees of freedom, because the overlapping variances are not independent. How-

ever, this does not mean that we cannot use it for improving our estimate of the true two-sample variance, because the estimators are positive and unbiased [77]. When studying the asymptotic behavior of  $S_y(f)$ , to characterize drift and noise in time series signals most frequently the  $\tau$ -overlap estimate is used as a trade-off between statistical independence and a smooth  $\sigma/\tau$  plot. As a summary the different estimates for the two-sample variance are illustrated in Fig. 2 and can be calculated as

$$\begin{aligned} \sigma_{y_{no}}^2(\tau) &= \frac{2}{M} \sum_{i=1}^{M/2} \frac{(\bar{y}_{2i+1} - \bar{y}_{2i})^2}{2} \quad \text{non-overlap} \\ \sigma_{y_{\tau o}}^2(\tau) &= \frac{1}{M-1} \sum_{i=1}^{M-1} \frac{(\bar{y}_{i+1} - \bar{y}_i)^2}{2} \quad \tau\text{-overlap} \quad (19) \\ \sigma_{y_{mo}}^2(\tau) &= \frac{1}{M-2k+1} \sum_{i=1}^{M-2k} \frac{(\bar{y}_{i+k} - \bar{y}_i)^2}{2} \quad \text{max-overlap} \end{aligned}$$

With the definitions and relationships derived above the variance of time series data can be analyzed in cases where the classical variance cannot be applied anymore. The combination of the moving average low-pass filter  $L(f)$  with the first order derivative high-pass filter  $H(f)$  forms a band-pass filter  $B(f)$  and the two-sample variance can be expressed as the variance of the output of band-pass filters applied to the signal under study  $y(t)$ . The variation of the integration time forms a band-pass filter with different bandwidth, which in signal processing is called a filter bank. This analysis is similar to a multi-resolution wavelet analysis [78] using the Haar mother wavelet [79]. A wavelet is defined as a set of functions  $\psi_{a,b}(t)$  derived from a function  $\psi(t)$  by dilation and translation [80],

$$\psi_{a,b}(t) = \frac{1}{\sqrt{|a|}} \psi\left(\frac{t-b}{a}\right) a \neq 0, \quad a, b \in \Re \quad (20)$$

where  $a$  is a scale parameter used to control the dilation,  $b$  is a shift parameter used to control the translation, and  $\psi(t)$  is called the mother wavelet function. The wavelet transform is defined as the projection of a signal  $y(t)$  on the wavelet

$$W_\psi(a, b) \equiv \frac{1}{\sqrt{|a|}} \int_{-\infty}^{+\infty} y(t') \psi\left(\frac{t'-b}{a}\right) dt \quad (21)$$

This can be seen as a convolution of the wavelet  $\psi_{a,b}(t)$  with the time series  $y(t)$ . In 1910 Haar has described an orthogonal system, which in wavelet analysis is now called the Haar wavelet [81]

$$\psi_{\text{Haar}}(x) = \begin{cases} +1 & 0 \leq x < \frac{1}{2} \\ -1 & \frac{1}{2} \leq x < 1 \\ 0 & \text{elsewhere} \end{cases} \quad (22)$$

If we substitute  $x = \frac{t'-b}{a}$  we obtain on intervals  $[b, b+a]$

$$\psi_{\text{Haar}}\left(\frac{t'-b}{a}\right) = \begin{cases} 1 & b \leq t' < b+a/2 \\ -1 & b+a/2 \leq t' < b+a \\ 0 & \text{elsewhere} \end{cases} \quad (23)$$

The computation of the Allan variance can be seen as of a convolution of the signal  $y(t)$  by a Haar wavelet if we substitute in (23)  $a = 2\tau$  and  $b = t$  and we obtain for the Haar wavelet coefficients

$$\begin{aligned} W_{\psi_{\text{Haar}}}(a, b) &= \frac{1}{\sqrt{|a|}} \int_{-\infty}^{+\infty} y(t') \psi_{\text{Haar}}\left(\frac{t'-b}{a}\right) dt' \\ &\stackrel{(23)}{=} \frac{1}{\sqrt{|a|}} \left[ \int_b^{b+a/2} y(t) dt' - \int_{b+a/2}^{b+a} y(t) dt \right] \\ &\stackrel{(2)}{=} \sqrt{\frac{\tau}{2}} [\bar{y}(t) - \bar{y}(t+\tau)] \end{aligned} \quad (24)$$

The wavelet variance can be defined as the average of the squared wavelet transform (21) over the translation index  $b$  for constant dilatation index (scale)  $a$  as

$$\begin{aligned} \sigma_{\text{Haar}}^2(a) &= \langle W_{\psi_{\text{Haar}}}^2(a, b) \rangle_b \\ &= \tau \cdot \frac{1}{2} \langle (\bar{y}(t+\tau) - \bar{y}(t))^2 \rangle = \tau \cdot \sigma_y^2(\tau) \end{aligned} \quad (25)$$

The transition from continuous to discrete coefficients  $W_{\psi_{\text{Haar}}}^2(a, b) \rightarrow d_{j,k}^2$  by substituting the scale  $a = \tau_0 \cdot 2^k$  and dilatation  $b = j \cdot \tau_0 \cdot 2^k$  defines on the interval  $[j \cdot \tau_0 \cdot 2^k, (j+1) \cdot \tau_0 \cdot 2^k]$  the two-sample (Allan) variance at scale  $k$  as

$$\sigma_y^2(k) \stackrel{(25)}{=} \frac{1}{k} \frac{1}{M} \sum_{j=1}^M d_{j,k}^2 = \frac{2}{N} \sum_{j=1}^{\frac{N}{2k}} d_{j,k}^2 \quad (26)$$

calculated from  $M = N/2k$  non-overlapping subgroups of  $N$  time series data sampled at intervals  $\tau_0$ . This is an alternative estimator for the Allan variance and the wavelet variance at scale  $k$  turns out to be equal to half the non-overlap Allan variance [82].

In practical applications ‘Sigma/Tau’, ‘ $\sigma/\tau$ ’ or ‘Allan’ plots are investigated after an estimate of the two-sample variance has been calculated. These plots provide much more information than the analysis of noise types in frequency stability analysis or the optimum averaging time derived from the first minimum in the plot. Actually, some further and in-depth information for spectroscopic applications is contained in  $\sigma/\tau$  plots as shown in Fig. 3a. Such a plot can be expected from a well-designed spectrometer, whenever a stable calibration gas is supplied. The fundamental contributions from white noise and drift can be observed in the lower curve, while in the upper curve flicker noise is included. The origin of the drift and other characteristic

features of the  $\sigma/\tau$  plot will be discussed in the following sections in detail and the discussion here is limited to the typical time constants. The minimum in the  $\sigma/\tau$  plot is an estimate for the stability time and it is important to mention that this is the maximum time available for a complete measurement cycle. This means that all necessary measurements must be completed within this time interval, which includes exchange times of gases when switching between calibration gas, zero air for background measurements and the ambient air sample. As a consequence the effective time available to improve the precision of the measurement is less than half of the maximum integration time  $\tau_{\text{max}}$  determined from the first minimum of the  $\sigma/\tau$  plot [11]. The underlying assumption is that, in order to remove drift effects, differences of the sample spectra minus background spectra have to be calculated. It is obvious that both spectra should have the same signal-to-noise ratio and therefore require the same signal averaging time. When random noise dominates the measurements the plot will follow the  $1/\tau$  slope as indicated by the dashed line. As long as the variance stays on this line, the two-sample variance is equal to the white noise variance of the mean (18). In this case the precision gets better (lower) while the accuracy remains constant. As soon as the two-sample variance deviates from this line due to flicker noise or drift influence the precision improves less than expected but in turn the accuracy gets worse because the deviation between the measured and the true value increases. If accuracy is the issue, then  $\tau_{\text{acc}}$  defines the limit for signal averaging, while  $\tau_{\text{max}}$  determines the final limit for the precision that can be reached. In general  $\tau_{\text{acc}} \ll \tau_{\text{max}}$  and it can be seen from the two traces in Fig. 3a that flicker noise has a severe influence on the stability of the accuracy, but not on  $\tau_{\text{max}}$ . The choice of the appropriate stability time depends critically upon the application and the measurement requirements in terms of precision and accuracy.

There are cases where hard- or software signal conditioning is applied during the measurement process. The  $\sigma/\tau$  plot in Fig. 3b illustrates the effect of low- and high-pass filtering, which usually are investigated in the frequency domain, but can be observed in the time domain as well. A typical low-pass filter characteristic can be obtained electronically, by software signal smoothing or caused by a damping effect of fast concentration changes or fluctuations due to limitations in the gas sampling system [83, 84]. The equivalent effect of high-pass filtering can be caused by ac signal coupling or a ‘trend removal’ procedure [74]. Fig. 3c shows a ‘shoulder’ as another characteristic feature, which can be found in  $\sigma/\tau$  plots when alternating signal/background measurements or gas concentration difference measurements under optimized measurement cycles have to be used in high sensitivity applications [11]. The need for comparable signal-to-noise ratios when making difference measurements as described above introduces

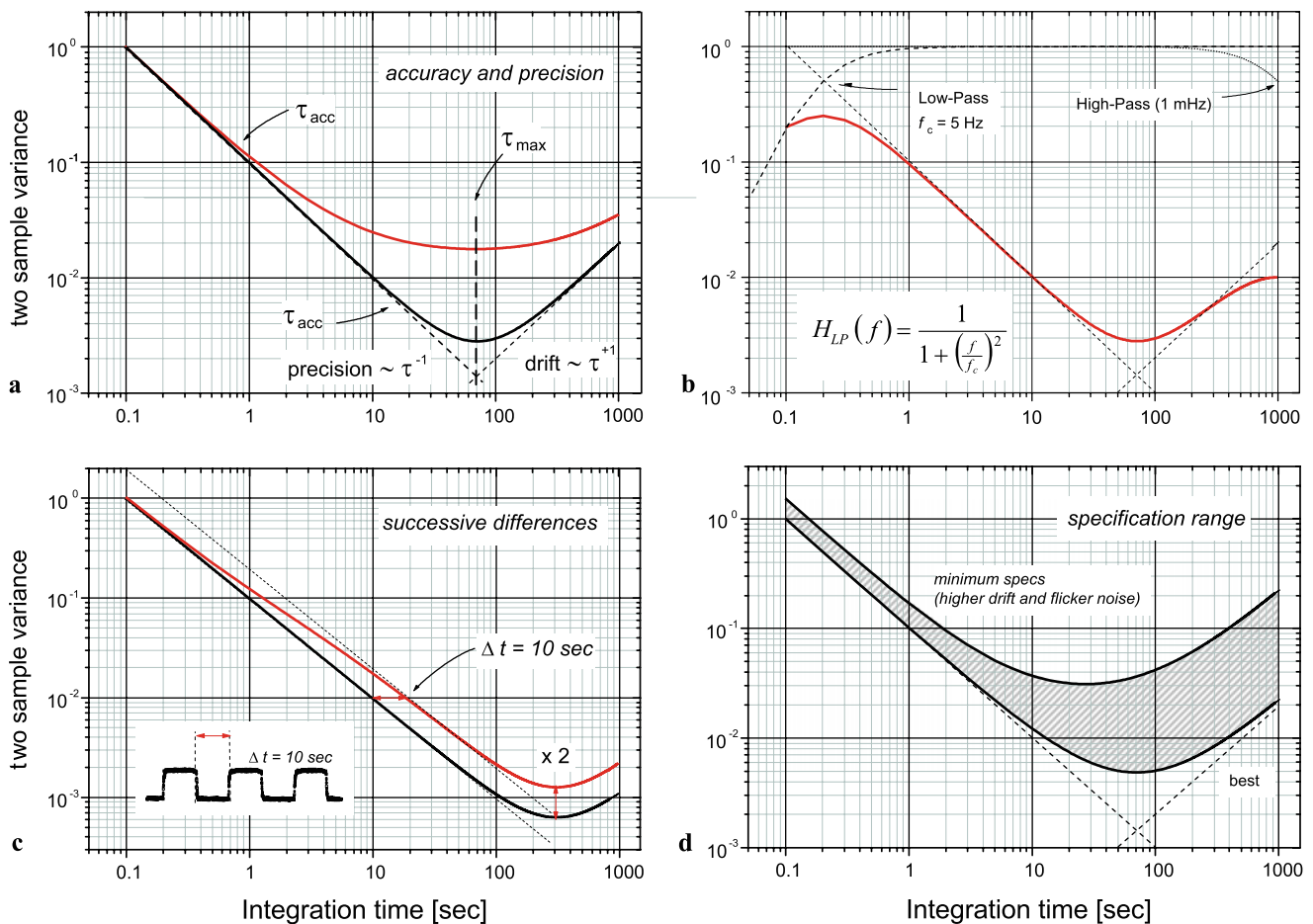


**Fig. 3** A typical  $\sigma/\tau$  plot from a calibration (a) with contributions from drift and white noise. The upper curve includes additional flicker noise, which affects the stability of the accuracy  $\tau_{\text{acc}}$ , but not the location of the minimum at  $\tau_{\text{max}}$ . (b) The two-sample variance from a

high-pass/low-pass filtered time series and (c) from difference measurements with the characteristic ‘shoulder’ due to a duty cycle effect [27]. (d) Instrument uncertainty can be expressed as a range of  $\sigma/\tau$  plots, recorded under different environmental conditions.

duty cycle effects as discussed by Werle et al. [27]. Taking differences from successive measurements requires at least twice the averaging time. Therefore the dashed white noise line and correspondingly the expected minimum are shifted in the vertical direction (if a dead time due to switching can be neglected) compared to non-differential measurements. The ‘shoulder’ located at the end of the sampling time for the first of the two measurements can also be found in typical ‘delta’ measurements in stable isotopes infrared spectroscopy [44, 47]. For continuous monitoring applications under changing ambient conditions it is more realistic and reliable to specify a range [43] rather than a single  $\sigma/\tau$  curve and it is advisable to check the system stability status to be within these specifications on a regular basis. A typical range of  $\sigma/\tau$  plots from a non-optimum scenario to best performance is shown in Fig. 3d.

### 3 Optical fringes and long-term stability

In practice most laser spectrometers suffer from an unwanted etalon effect frequently called fringing. The effect comes from plane-parallel surfaces in the laser beam, which may act as a frequency filter through the interaction of multiple reflections from the partially reflecting surfaces with reflectivity  $R$  forming a resonator. The multiple output beams differ in phase  $\delta$  due to the different path lengths traversed by each of the beams. The transmission of an etalon (Fig. 4a) is described by the Airy formula

$$I_T = \frac{1}{1 + \frac{4R}{(1-R)^2} \cdot \sin^2\left(\frac{\delta}{2}\right)} \quad (27)$$

The elementary theory of the Fabry–Pérot etalon is described in detail in the literature [85]. This brief summary will describe how the etalon acts as a simple filter for changing optical frequency into transmitted intensity. If we as-

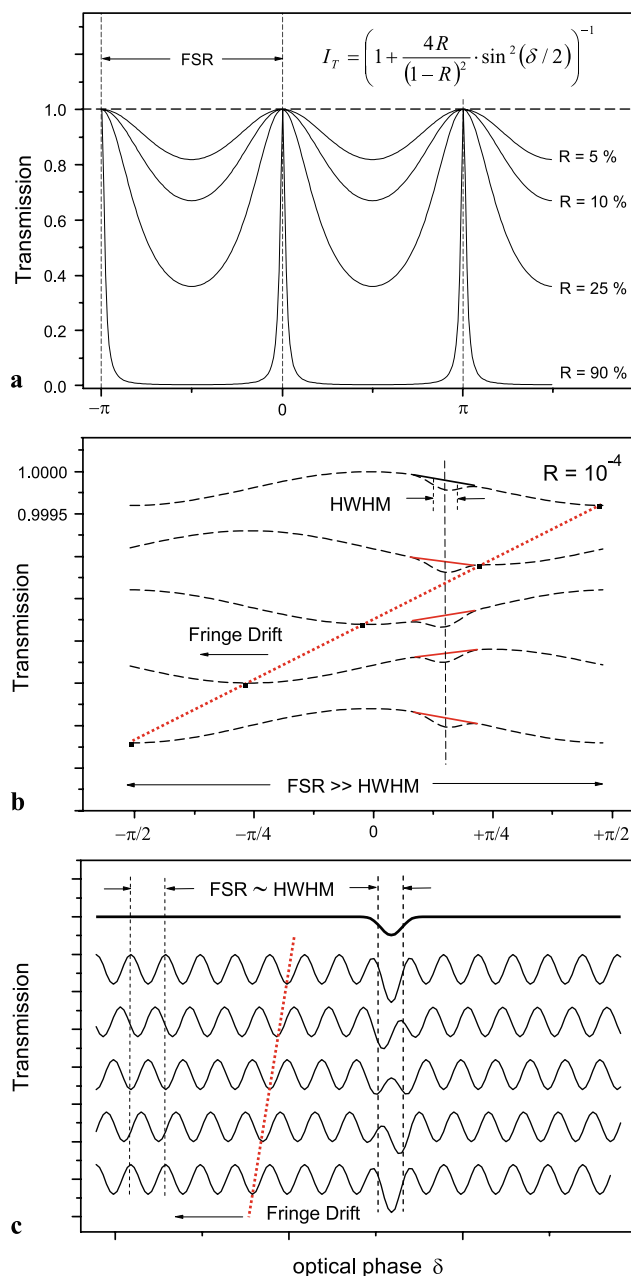


**Fig. 4** (a) Airy function for different reflectivity of the cavity surface (b) A fringe drift causes a time dependent background change when the free spectral range (FSR) is greater than the half width at half maximum (HWHM) of the spectral line under investigation. (c) For a FSR comparable to the HWHM a time dependent variation of the true signal amplitude can be observed

sume normal incidence to simplify the discussion, the optical phase  $\delta$  acquired by the light during one round trip through the etalon is given by  $\delta = 4\pi \cdot n \cdot d/\lambda$  where  $\lambda$  is the wavelength of the laser,  $d$  is the distance of the surfaces forming the etalon,  $n$  is the index of refraction. The transmission peaks of the etalon described by the Airy formula have a maximum when the phase difference for a round trip  $\delta = 2\pi \cdot 2 \cdot n \cdot d/\lambda_m = 2\pi \cdot m$  is an integer multiple  $m$  of  $2\pi$ .

Expressing the maximum condition in terms of frequency gives a more useful expression for the location of transmission peaks  $\nu_m = m \cdot c/2 \cdot n \cdot d$ . With the frequencies of the maximum transmission peaks known, the frequency separation between successive peaks can be calculated. The peak-to-peak separation in frequency is known as the *free spectral range (FSR)*

$$\text{FSR} = \nu_{m+1} - \nu_m = \frac{c}{2 \cdot n \cdot d} \quad (28)$$

At normal incidence, the frequency spacing between maximum transmission peaks in an ideal etalon depends inversely on the index of refraction,  $n$ , times the thickness,  $d$ . The product of these two values,  $n \cdot d$ , is the optical path length, which determines the peak locations for a given frequency, while the reflectivity of the etalon determines the shape of the peaks. The higher the resonators reflectivity is the narrower is the observed peak. The shape of the etalon transfer function is commonly characterized by the finesse  $F = \pi\sqrt{R}/(1-R)$ . A finesse of  $F = 100$  requires a reflectivity of 97%. Jennings proposed that such an etalon cavity might also be used as a sample chamber to increase the effective optical path through the sample and found to enhance line absorptions by a factor of 20 [86]. If a single-mode laser is tuned to the slope of a high-finesse etalon any frequency deviation will lead to a change in the transmitted signal, which in turn can be used in a feedback loop to stabilize the laser frequency. With this scheme it is also possible to lock a laser to an external cavity for precision tuning in high-resolution molecular spectroscopy [87, 88]. While these applications require high-finesse etalons, usually in most spectroscopic systems unwanted etalons can be observed.

When looking at the design of typical spectrometers for field applications it is found that resonators may exist at different scales, from the laser crystal dimension of hundreds of microns up to about 100 m between the laser and the detector for systems using optical multi-pass cells. A laser beam may interact with the first window of its housing or focusing optics or with any parallel surface of transmissive optical elements in the laser beam path. Due to many possible resonator geometries the corresponding free spectral ranges may cover a wide range. With a refractive index of 1.49 for a 2 mm BaF<sub>2</sub> window we obtain a FSR of 50 GHz or 1.22 nm at 2.7  $\mu\text{m}$  ( $1.6 \text{ cm}^{-1}$ ) while for an air spaced etalon with reflecting surfaces separated by 20 cm we calculate a FSR of 750 MHz ( $0.025 \text{ cm}^{-1}$ ). Resonators corresponding to the typical path-length of 10 to 100 m in optical multi-pass cells have free spectral ranges of 15 and 1.5 MHz ( $0.005 \dots 0.0005 \text{ cm}^{-1}$ ). The free spectral range of the possible etalon structures spans over 5 orders of magnitude. In contrast to the high-finesse etalons, these unwanted

resonators usually have a very low finesse due to lower reflectivity  $R$  and, therefore, appear as a sine function when they can be observed during a spectral scan as fringes.

For trace gas sensing applications a selected absorption line is monitored by applying sensitive detection techniques to measure the absorption in the optical path and depending on the application the detection limits are ranging from  $10^{-4}$  down to  $10^{-6}$ . A reflectivity of 0.1% ( $F = 0.1$ ) results in a peak-to-valley variation of the etalon transfer function from 1 to 0.996 or  $4 \times 10^{-3}$  and any variation in the transfer function of the etalon can have a significant impact on the system performance. In general any spectroscopic instrument cannot be considered as perfectly stable and we may observe time dependent changes of surface reflectivity  $R(t)$ , laser wavelength  $\lambda(t)$  and resonator separation  $d(t)$ . It is obvious that an instrument for field measurements outside the well defined laboratory conditions can be much more influenced by such effects. The reflectivity may change due to the contact with ambient air and such a “pollution effect” may lead to a unidirectional long-term trend in the etalon transfer function. Variations in the laser wavelength with time depend on the quality of the line locking, the laser driver electronics and aging. Variation of the spectrometer temperature due to heating or an air condition system modulate the resonator separation  $d$  and, therefore, may lead to a bidirectional modulation of the transfer function similar to thermal effects with daily, seasonal or annual cycles. While fringes corresponding to very short resonators have a large FSR or periodicity in the spectral domain, fringes originating from longer optical structures appear as high-frequency interference to the desired signal. Fortunately, these interferences can be attacked by appropriate low-pass filtering. As critical remain the fringes with broad structures (Fig. 4b) or with a free spectral range in the order of the linewidth (Fig. 4c). Depending on the relative position of the spectral feature under investigation to the transmission peaks of the etalon an apparently linear looking, positive or negative slope or even a curved baseline may be superimposed to the undisturbed measurement signal. In addition fringes in general do not show a constant spacing due to non-linear tuning curves of semiconductor lasers. Finally, several independent etalon induced effects can be superimposed and lead to complex and time dependent interference fringes.

Many attempts have been published to cope with the fringe challenge. In principle the unwanted background fringe structure could be recorded and subtracted from the subsequent spectral scans before the spectra are further analyzed [89]. This requires detailed knowledge about the relevant time scales for essential changes in the fringe pattern and obviously depends on the magnitude of interfering fringes relative to the absorption line used for the measurement. It turns out that the signal-to-fringe ratio is more important for the system performance than the signal-to-noise ratio. In order to define the calibration timescale for

efficient fringe suppression [11], the two-sample variance can be used to describe system stability in the presence of optical fringes. There are many sources of noise and drifts in a laser spectrometer. The fundamental random noise contributions like detector thermal noise and shot (quantum) noise [90, 91] are not the key issue with the electronic components available, and as they usually are band-limited and have a frequency independent white spectrum they can easily be averaged down with time and are related to the instrument’s precision. Detector noise and laser wavelength drift can be reduced by cooling and careful selection processes and line-locking [3]. More cumbersome for field applications are non-random noise contributions which include opto-mechanical drifts due to ambient pressure and temperature changes, which in turn generate time dependent fringes. As mentioned before, in cases when the time-varying background has a similar structure as the spectral absorption line under investigation fringes are difficult to suppress. Fringe background structures can be found in all spectrometers using multi-pass cells and cavity ring down systems [92] and cannot be eliminated by simple filtering. If etalons were stationary they could be subtracted and would simply represent an offset in the total absorption measurement. However, since they can vary during averaging time scale they will be interpreted as signal change as their amplitude and/or phase changes (Fig. 4b/c). The challenge of suppressing etalon fringes was recognized decades ago and many hardware and software attempts have been made since then to reduce the impact of fringes [93–95]. Careful optical design and alignment are a prerequisite to avoid excessive etalon effects. Anti-reflection coatings, the use of reflective as opposed to transmissive optics, tilted or wedged optics may help to keep etalon fringes to a minimum. Astigmatic optical multi-pass cells have been developed [96, 97] and matching the input beam to the cell mode ensures a minimal beam size within the cell and gives low levels of interference fringes [98]. Frequent calibrations for in-situ measurements in cells are also used to minimize the effect of drifts. Mechanical approaches to cope with fringes like the Brewster plate spoiler try to smear out the fringes and reduce the coherence by vibrating an optical element [99]. For a single dominant fringe whose structure does not change significantly over time this approach can be very useful. Software methods apply digital signal processing to filter to suppress fringes. Digital filters [11, 100–102] can be effective in reducing the effect of fringes however they do have their limitations as an unwanted background structure usually includes several fringes with different dependence on temperature, pressure, and other factors.

The power spectral density of a single optical fringe observed in a spectrometer can be described as  $S_y(f) = \delta(f - f_{\text{Fringe}})$  and is shown in Fig. 5a. For comparison

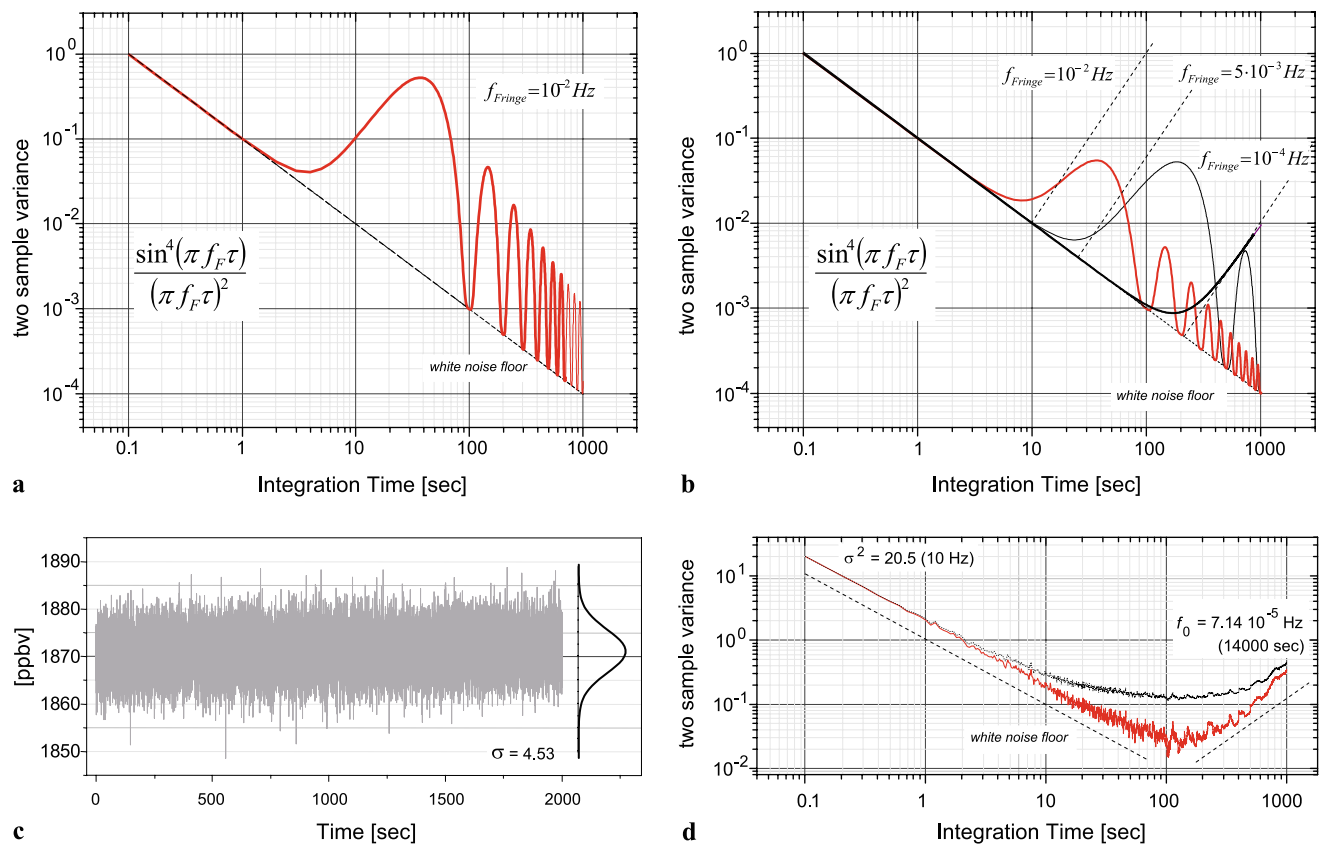


**Fig. 5** (a) Analysis of a time series signal with equivalent contributions from white noise and a fringe at  $f_F = 1/100$  Hz compared to (b) a factor of 10 lower fringe amplitude (c) Half hour time series data

with a small drift of  $1/14000$  Hz and (d) corresponding  $\sigma/\tau$  plot. The lower curve corresponds to white noise plus a fringe, while in the upper curve  $1/f$  noise is included

in Fig. 5b a fringe with the same frequency but ten times higher noise-to-fringe ratio is displayed in the frequency domain in terms of the two-sample variance together with 2 slower fringes of same amplitude. The dashed lines indicate the expected behavior for a linear drift and the slowest fringe with a period of 10000 sec appears as such a linear drift. In practice, the laser frequency tuning is not linear and several fringes may be superimposed to generate beat frequencies so that the overall situation can be very complicated and the fringe structure in the  $\sigma/\tau$  plot can be less clear than shown here. Some fringes will have a free spectral range comparable to the width of the absorption profile, which makes it impossible to filter out fringes without affecting the absorption signal. Figure 5c shows half an hour of time series concentration data with a very slow fringe of approx. 14000 sec superimposed. Figure 5d illustrates the corresponding Allan plot for the case of white noise and drift (lower curve). In this case the fringe free spectral range is large making it difficult to determine its frequency and phase and devise an effective filter. In the presence of optical feedback [103] the upper curve with  $(1/f)$  flicker noise added will be observed. Finally, it should be noted that phase noise and refractive index fluctuations in optical multi-pass

cells may also affect the overall spectrometer performance, especially when phase sensitive detection techniques like the high-frequency modulation technique is applied [104]. In general, there is no way to eliminate fringes in optical systems completely. Recently Dyroff et al. [29] reported a fringe suppression technique based on the Stark effect in molecular spectra. A periodic high voltage modulation has been applied to the target gas in an optical multi-pass cell. This modulation acts only on the molecular absorption line, but does not affect the background fringe structure and therefore a fringe free signal can be obtained. This method is a technical challenge and unfortunately works only with selected polar molecules like formaldehyde or hydrogen peroxide. As a consequence for the most wanted molecules for field measurements in atmospheric research like  $\text{CH}_4$ ,  $\text{N}_2\text{O}$ ,  $\text{H}_2\text{O}$  and  $\text{CO}_2$  isotopes for example, fringes will continue to appear in all types of spectrometers and remain cumbersome when making field measurements [105]. Therefore, frequent calibration is the best choice to assure the accuracy of gas measurements and the time scale for the recalibration has to be determined from a  $\sigma/\tau$  analysis [11].

#### 4 Atmospheric turbulence and short-term stability

Integrated ecosystem-atmosphere process studies provide a better understanding how the interacting physical, chemical and biological processes transport matter through the land-atmosphere interface from the cell level to a global scale. The eddy-covariance technique [106–108] directly determines the flux of an atmospheric trace constituent through a plane parallel to the surface. For the determination of surface emission and deposition fluxes, the method is rigorous when specific criteria are met and the meteorological conditions controlling the state of the turbulence should not vary over the course of the measurements, which is Taylor's assumption of 'frozen turbulence' [106, 109]. Because the eddy correlation method measures the instantaneous upward or downward transport of trace gases and then averaging contributions to give the net flux, it must take into account the frequency range of the turbulence for vertically transporting the constituents in the atmosphere to avoid losses in the calculation. The turbulent flow consists of vortices and the flow in every vortex is made of smaller vortices, down the scale to the point when the viscosity of the fluid dissipates the kinetic energy of motion into heat. If there is no influx of energy, the energy of the motion will eventually dissipate and therefore it can be assumed that the energy flow is balanced [110]. The motion of a liquid is made of waves of different lengths and Kolmogorov asked the question, what is the share of energy carried by waves of a particular length? Among the quantities involved, first, we have the energy flow (it is the same as the dissipation of energy). According to the kinetic energy  $K = mv^2/2$  of a moving particle, the dimension of energy is  $\text{mass length}^2/\text{time}^2$ . It is convenient to make all calculations per unit of mass and then the energy flow  $\varepsilon$  has the dimension  $\text{energy}/(\text{mass time}) = \text{length}^2/\text{time}^3$ . If we use the number of waves fitting into the unit of length, the wave number  $\kappa$  has dimension  $1/\text{length}$ . Then the energy spectrum  $E(\kappa)$  is the quantity such that, given the interval  $\Delta\kappa = \kappa_1 - \kappa_2$  between the two wave numbers, the energy per unit of mass carried by waves in this interval should be approximately equal to  $E(\kappa_1)\Delta\kappa$ . Hence the dimension of  $E$  is  $\text{energy}/(\text{mass wave number}) = \text{length}^3/\text{time}^2$ . Kolmogorov made the key assumption that '*the way bigger vortices are made from smaller ones is the same throughout the range of wave numbers, from the biggest vortices (like a cyclone covering the whole continent) to a smaller one (like a whirl of dust on a street corner)*'. Then the energy spectrum  $E$ , the energy flow  $\varepsilon$  and the wave number  $\kappa$  are linked by an equation which does not involve anything else. Since the three quantities involved have completely different dimensions, we can combine them only by means of an equation of the form  $E(\kappa) \approx \alpha_k \varepsilon^x \kappa^y$ . Here  $\alpha_k$  is a constant; since the equation should remain the same for small scale and for global scale events, the shape of the equation should

not depend on the choice of units of measurements, hence  $\alpha_k$  should be dimensionless. Equating lengths with lengths and times with times, we have  $\text{length}^3 = \text{length}^{2x} \cdot \text{length}^{-y}$  and  $\text{time}^2 = \text{time}^{3x}$ , which leads to two linear equations in  $x$  and  $y$ ,  $3 = 2x - y$  and  $2 = 3x$ . This gives us  $x = 2/3$  and  $y = -5/3$  and we obtain Kolmogorov's law for the inertial subrange

$$E(\kappa) \approx \alpha_k \varepsilon^{2/3} \kappa^{-5/3} \quad (29)$$

The dimensionless constant  $\alpha_k$  is called the Kolmogorov constant and can be determined from experiments and is in the range from 1.53...1.68 [106]. The easiest way to determine whether any measured spectrum has an inertial subrange is to plot the spectrum ( $S$  vs.  $\kappa$ ) on a log graph. The inertial subrange portion should then appear as a straight line with a  $-5/3$  slope. Such a behavior of frequency spectra has been observed for turbulence spectra [111] up to the dimensions of interplanetary magnetic fields [112]. According to Taylor's hypothesis of frozen turbulence frequencies are related to wavenumbers  $f = \bar{u} \cdot \kappa$ , where  $\bar{u}$  is the mean horizontal wind speed [106].

In order to resolve the inertial subrange in the frequency spectrum, time series measurements at typically 10 Hz are necessary. Therefore, the eddy-covariance technique requires simultaneous fast and accurate measurements of the vertical velocity and the concentration of the trace species in question. Laser spectroscopy has proven to be the appropriate measurement technique for field measurements with the responsiveness and sensitivity required for direct eddy correlation flux measurements. Historically most instruments used for greenhouse gas flux measurements were research type spectrometers modified for field applications [113–119] and measurements were conducted by the system developers or in close cooperation. Improvements in the quality of semiconductor lasers have finally led to the development of a new generation of diode-laser spectrometers and a growing selection of commercial instrumentation for atmospheric research and trace gas flux measurements is available and increasingly being used in ecosystem research for greenhouse gas monitoring and flux measurements [120–127]. All these laser-optical greenhouse gas measurements are based on commercially available laser spectrometers for nitrous oxide, methane and carbon dioxide including isotopes. The standard procedure for computing eddy-covariance fluxes using a trace gas analyzer and a sonic anemometer is a Reynolds decomposition of a time series of the vertical wind speed  $w$  and the trace gas mixing ratio  $c$  into a mean and a perturbation component as  $c = \bar{c} + c'$  and  $w = \bar{w} + w'$  where the overbar denotes block time averaging assuming a constant perturbation time scale [106]. The flux  $F$  can be determined with the direct eddy-correlation method by the calculation of the covariance of the two measured quantities  $w$  and  $c$  of a time se-

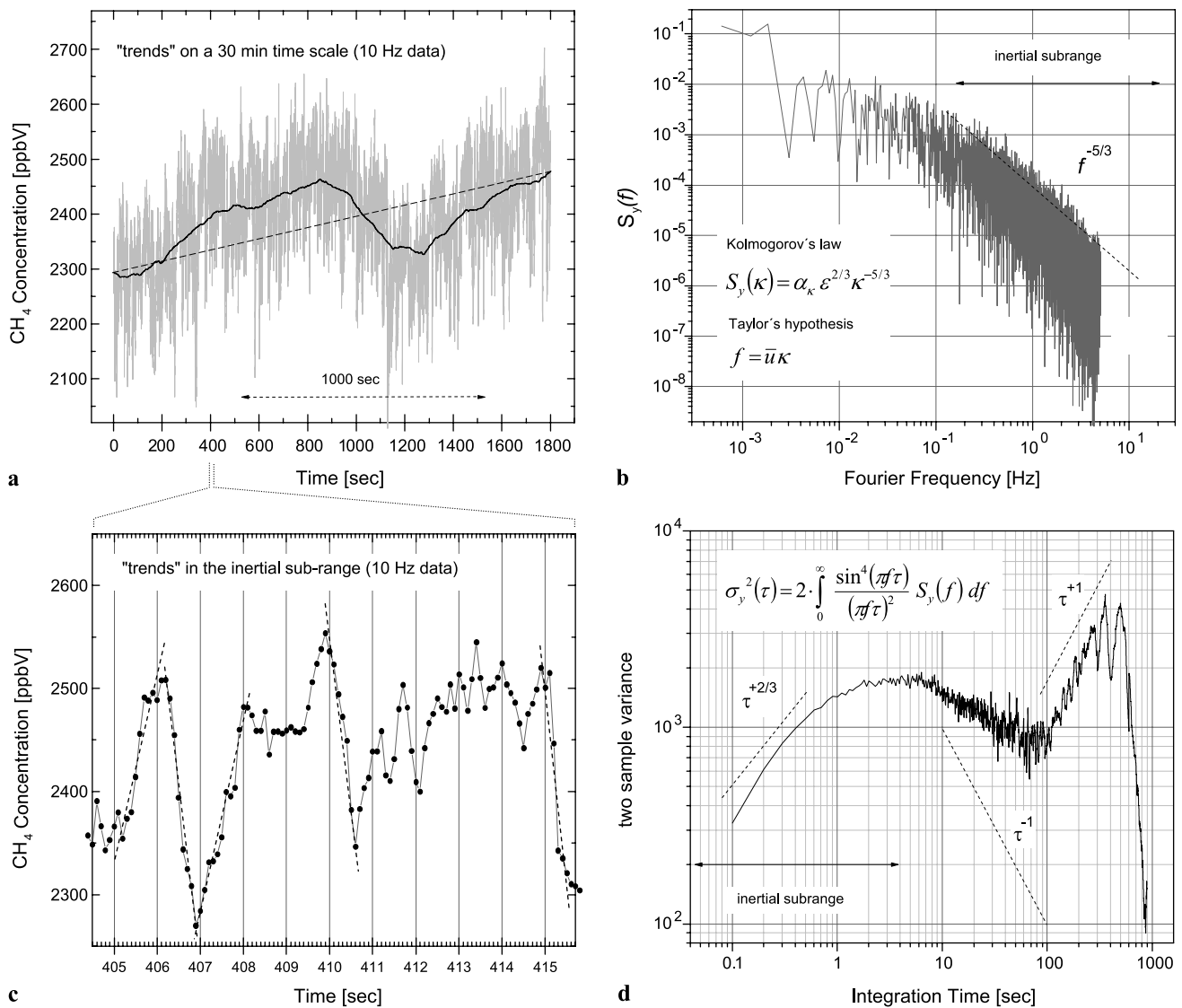


**Fig. 6** (a) Methane concentration in ambient air recorded during field measurements [67] with a time resolution of 10 Hz over 30 min. (b) Kolmogorov’s  $-5/3$  frequency dependence in the inertial subrange can be seen in the Fourier spectrum. (c) Short-term ‘trends’ due to turbulence can be observed after zooming into the time series. (d) The  $\sigma/\tau$  plot includes the features in of the frequency spectrum above, but also provides information about the long-term behavior [74].

ries as  $\langle F \rangle = w'c'$  where the brackets denote time averaging over the record length (flux averaging time scale). Obviously the choice of the time scale sets an upper limit on the range of scales included in the computed flux. To control the data quality, stationarity has to be assured during the averaging interval. An ambient time series is shown in Fig. 6a where atmospheric methane has been recorded at 10 Hz for about 30 min. A 300 sec moving average and a linear slope background are superimposed to the time series data to illustrate possible trends. Trend removal in such time series data is an issue for the Reynolds decomposition and various procedures have been discussed in the literature [107]. In this context, the two-sample variance has been used as a tool to determine a filter time constant and

the need for an optimized calibration cycle has been discussed [71, 74]. The frequency spectrum of the time series is displayed in Fig. 6b and the expected Kolmogorov  $-5/3$  frequency dependence in the inertial subrange can be seen [111] together with a very small attenuation at the high-frequency cut-off due to an additional low-pass filtering caused by the gas sampling system [83, 84]. A closer look into a short interval of the time series resolved at 10 Hz is shown in Fig. 6c. At this scale (non-linear and linear) short-term ‘trends’ can be observed due to turbulence in the inertial subrange and therefore a similar behavior with respect to averaging can be expected as for the long-term drift already discussed. The time-domain characterization

based on a two-sample variance using a  $\sigma/\tau$ -plot shown in Fig. 6d provides the same information as the spectral characteristics of turbulence in the frequency domain [74, 111]. Atmospheric turbulence is resolved for averaging intervals below 1 sec ( $f^{-5/3} \leftrightarrow \tau^{+2/3}$ ) and appears as a drift seen on a time scale, which corresponds to the inertial subrange. The small high-frequency damping can also be identified for very short integration times. For increasing averaging times flicker noise from the laser [91, 103] and electronic components dominate and the two-sample variance remains at a constant level ( $f^{-1} \leftrightarrow \tau^0$ ). White noise dominates at longer integration time because fast fluctuations contribute less to the variance and averaging leads to a decreasing variance. The expected white noise ( $f^0 \leftrightarrow \tau^{-1}$ ) is overlaid by a peak for time scales of a minute and longer before the two-sample variance approaches again the white noise limit. During ambient measurements such a behavior can be caused for two reasons: The first possibility is that the stationarity of the measurement conditions is no longer valid and a drift is superimposed to a constant ambient concentration. This can be caused for example by an optical fringe as discussed in the previous section and illustrated in Fig. 5a/b. The alternative is a true variability in the ambient concentration, while the system itself remains stable and does not affect the measurement accuracy. Finally, any combination of both situations is possible as well and, therefore, it is important to understand the system characteristics and there is a need to separate instrumental effects from real sample signals. This is a major concern not only for concentration measurements but also for trace gas flux measurements. The increase in the two-sample variance at larger integration times could also be caused by coherent atmospheric structures or large eddies, which contribute to the gas exchange between the biosphere and atmosphere at longer time scales [107, 128, 129]. We have seen that the two-sample (Allan) variance can be used as an estimator for the Haar wavelet variance and vice versa and atmospheric data have been investigated using the Haar wavelet [130]. Taylor's frozen turbulence hypothesis [109] can be used to convert from time scales  $\tau$  to length scales  $s$ . An instrument installed on a fixed tower records the turbulent variables as the flow passes the sensor with a mean wind speed  $\bar{u}$  and we can convert from time increments to space increments using  $s = \bar{u} \cdot \tau$ . Concentration fluctuations due to such coherent atmospheric structures and optical fringes may have the same effect on the two-sample variance and therefore a prerequisite for the data interpretation is a periodic instrument recalibration [11] because then the resulting segmented dataset, after concatenation, can be used for eddy-covariance measurements [74].

## 5 Summary and conclusions

The two-sample variance is the square of differences of successive averages over a time scale  $\tau$  calculated from a record of time series data. In the frequency-domain a definition can be expressed as well, because the full information on the statistical properties is contained in the *power spectrum of the time series data*. The *Allan variance* can be seen as the filtered average of the *power spectral density of the time series* weighted with the filter function  $\sin^4(\pi f \tau)/(\pi f \tau)^2$ . Drift characteristics influencing a signal can be determined by analyzing the average structure of the power spectrum using a 'constant  $Q$ ' band-pass filter, where the ratio of the pass-band center frequency and width is fixed. Therefore, the procedure can be seen as a multi-resolution scale wavelet analysis using the Haar wavelet basis function. The *two-sample variance* represents the integral information over the power spectrum and gives a better statistical significance for the drift behavior than a single point in the *power spectrum*. In addition, it allows easy discrimination between different contributions to the signal, such as random noise, flicker noise and a long-term linear or periodic drift. This property makes it useful for the analysis of drift in spectroscopic data and double logarithmic  $\sigma/\tau$  plots are a convenient way to characterize the performance of a measurement system. When random noise dominates the measurements the curve will follow a  $1/\tau$  slope as expected for the variance of the mean and therefore gives an estimate for the precision of the averaged measurement. Under this condition the precision in the sense of Gauss (standard deviation) improves with averaging time, while the accuracy remains constant. When flicker noise (for example due to optical feedback from the laser or any drift from slow fringes) is superimposed to the signal, the two-sample variance deviates from the expected  $1/\tau$  line. Then the precision improves less than expected, but the deviation between the measured and the true value increases because the measurement accuracy gets worse. Therefore, when accuracy is an issue, the stability scale to be considered for signal averaging is always significantly lower than the commonly used maximum integration time  $\tau_{\max}$  derived from the minimum in the  $\sigma/\tau$  plot. Flicker noise generates a constant offset to the variance and therefore has an influence on the stability of the accuracy expressed by  $\tau_{\text{acc}}$ , but not on  $\tau_{\max}$ , which determines the limit for the precision that can be achieved. The choice of an appropriate stability time depends on the measurement requirements in terms of precision and accuracy for the given application and therefore needs some thought on how frequent the system has to be calibrated.

The concept discussed in this paper is recommended to characterize spectrometers in the laboratory prior to field measurements, check instrument performance at a field site and during campaigns and can be used to define a roadmap

for data quality assurance. The system specification can be documented for a range of environmental operating conditions. An optimized measurement cycle gives the required confidence about data quality and system stability and is recommended to distinguish sensor drift from true signals. As a consequence, an assessment of the system stability requires measuring a constant gas flow from a stable calibration gas source connected to the system inlet. Based upon such a characterization the influence of a modified system configuration or measurement conditions can be investigated. Plots of the two-sample variance from difference measurements based upon successive recordings of samples (isotopes, relaxed eddy-accumulation) display a ‘shoulder’ effect of the reduced duty cycle on the system performance and the first deviation from the  $1/\tau$  slope is a duty cycle effect and not an indicator for an accuracy problem. If the appropriate integration time and calibration cycle once has been determined for an instrument, it may be necessary to check its value from time to time. This is important especially under field operating conditions, where changes in parameters like temperature and pressure might change the fringe structure and therefore the accuracy of the measurement by superimposing artificial signals. A set of  $\sigma/\tau$ -plots recorded under different operating conditions allows the specification of uncertainty for the system as a range of expected performance. This is useful for continuous long-term control and monitoring applications, where automated self-checks can be utilized on a routine basis to check the system status. The two-sample variance analysis is also a useful tool for trace gas flux measurements using the eddy-covariance technique, because it can be used for a time-domain characterization of spectroscopic and micrometeorological data. The method can be applied to optimize the high-pass filter for a trend removal in time series data and can help to identify both, a possible high-frequency damping effect and low-frequency optical fringes. In the presence of atmospheric turbulence an ideal  $\sigma/\tau$  plot should start with an increasing two-sample variance, indicating that turbulence is resolved and after passing through a horizontal plateau, the two-sample variance should decrease with a slope of  $-1$  on a log-log scale. A periodic instrument recalibration is a prerequisite to distinguish between instrumental and atmospheric effects. If instrument effects are suppressed, any long-term behavior observed in the  $\sigma/\tau$ -plot can be attributed to a change in the trace gas concentration and may be caused by coherent structures.

The features of  $\sigma/\tau$  plots discussed in this paper go beyond the conventional analysis to determine a maximum integration time and provide additional information to spectral analysis in the frequency domain. Drift analysis of spectroscopic time series data based upon the two-sample (Allan) variance reviewed in this paper is easy to implement and a useful tool for a routine data quality check for both

new practitioners and experts in the field. Therefore, the approach might assist to ensure data quality for many field laser applications in industry and research.

## References

1. H. Schiff, G. Mackay, J. Bechera, *The Use of Tunable Diode Laser Absorption Spectroscopy for Atmospheric Measurements*. Air Monitoring by Spectroscopic Techniques, vol. 127, (Wiley, New York, 1994)
2. D. Brassington, *Tunable Diode Laser Absorption Spectroscopy for the Measurement of Atmospheric Species*. Advances in Spectroscopy, vol. 24 (Wiley, New York, 1995), pp. 83–148
3. P. Werle, *Spectrochim. Acta A* **54**, 197 (1998)
4. F.K. Tittel, D. Richter, A. Fried, in *Solid-State Mid-Infrared Laser Sources*, ed. by I.T. Sorokina, K.L. Vodopyanov, Topics in Applied Physics, vol. 89 (Springer, Berlin, 2003), pp. 445–510
5. P. Werle, in *Lasers in Environmental and Life Sciences—Modern Analytical Methods*, ed. by P. Hering, P. Lay, S. Stry (Springer, Heidelberg, 2004) pp. 223–243
6. A. Fried, D. Richter, in *Analytical Techniques for Atmospheric Measurements*, ed. by D. Heard (Blackwell Sci., Oxford, 2006), pp. 72–146
7. P. Werle, F. D’Amato, S. Viciani, in *Lasers in Chemistry—Probing Matter*, ed. by M. Lackner (Wiley-VCH, Weinheim, 2008), pp. 255–275
8. P. Werle, F. D’Amato *Appl. Phys. B* **92**, 303 (2008)
9. C.F. Gauss, Bestimmung der Genauigkeit der Beobachtungen (1816) (reprinted in C. F. Gauss Werke 4, Königliche Gesellschaft der Wissenschaften, Göttingen, 1880), pp. 109–117
10. J.W. Lindeberg, *Math. Z.* **15**, 211 (1922)
11. P. Werle, P. Mazzinghi, F. D’Amato, M. De Rosa, K. Maurer, F. Slemr, *Spectrochim. Acta Part A* **60**, 1685 (2004)
12. P.G. Moore, *J. Am. Stat. Assoc.* **50**, 270, 434 (1955)
13. J. von Neumann, R.H. Kent, H.R. Bellinson, B.I. Hart, *Ann. Math. Stat.* **12**, 153 (1941)
14. A. Hald, *Statistical Theory with Engineering Applications* (Wiley, New York, 1952)
15. W.M. Harper, *Biometrika* **54**, 419 (1967)
16. K. Shah, *Biometrika* **57**, 193 (1970)
17. J.A. Barnes, A.R. Chi, L.S. Cutler, D.J. Healey, D.B. Lesson, T.E. McCunigal, J.A. Mullen, W.L. Smith, R.L. Sydnor, R. Vesot, G.M.R. Winkler, *IEEE Trans. Instrum. Meas.* **IM-20**, 105 (1971)
18. D.W. Allan, *Proc. IEEE* **54**, 221 (1966)
19. J.A. Barnes, *Proc. IEEE* **54**, 207 (1966)
20. E.S. Ferre-Pikal, J.R. Vig, J.C. Camparo, L.S. Cutler, L. Maleki, W.J. Riley, S.R. Stein, C. Thomas, F.L. Walls, J.D. White, in: *Proc. of the Annual IEEE International Frequency Control Symposium* (IEEE Press, New York, 1997), pp. 338–357.
21. H. Marouani, M.R. Dagenais, *J. Comput. Syst., Netw. Commun.* **2008**, 583162 (2008)
22. R. Schieder, C. Kramer, *Astron. Astrophys. A* **373**, 746 (2001)
23. G. Wirtz, G. Sonnabend, R. Schieder, *Spectrochim. Acta A* **58**, 2457 (2002)
24. T.J. Witt, *IEEE Trans. Instrum. Meas.* **50**, 445 (2001)
25. D. Gambis, *Adv. Space Res.* **30**, 207 (2002)
26. D. DiPietroPaolo, H.P. Müller, S.N. Erné, *Phys. Med. Biol.* **50**, 2415 (2005)
27. P. Werle, R. Mücke, F. Slemr, *Appl. Phys. B* **57**, 131 (1993)
28. A. Joshua, V. Venkataraman, *Rev. Sci. Instrum.* **80**, 023908 (2009)
29. C. Dyroff, P. Weibring, A. Fried, D. Richter, J.D. Walega, A. Zahn, W. Freude, P. Werle, *Appl. Phys. B* **88**, 117 (2007)

30. H. Sabana, T. Fritsch, M. Boyomo Onana, O. Bouba, P. Hering, M. Mürtz, *Appl. Phys. B* **96**, 535 (2009)
31. A. Foltynowicz, W. Ma, O. Axner, *Opt. Express* **16**, 14689 (2008)
32. J. Skrinsky, R. Janeckova, E. Grigorova, M. Strizik, P. Kubat, L. Herecova, V. Nevrlý, Z. Zelinger, S. Civiš, *J. Mol. Spectrosc.* **256**, 99 (2009)
33. H. Cattaneo, T. Laurila, R. Hernberg, *Appl. Phys. B* **85**, 337 (2006)
34. A.A. Kosterev, F.K. Tittel, D.V. Serebryakov, A.L. Malinovsky, I.V. Morozov, *Rev. Sci. Instrum.* **76**, 043105 (2005)
35. E. Kerstel, L. Gianfrani, *Appl. Phys. B* **92**, 439 (2008)
36. E.H. Wahl, B. Fidric, C. Rella, S. Koulikov, B. Kharlamov, S. Tan, A.A. Kachanov, B.A. Richman, E.R. Crosson, B.A. Paldus, S. Kalaskar, D.R. Bowling, *Isot. Environ. Health Stud.* **42**, 21 (2006)
37. B. Tuzson, J. Mohn, M.J. Zeeman, R.A. Werner, W. Eugster, M.S. Zahniser, D.D. Nelson, J.B. McManus, L. Emmenegger, *Appl. Phys. B* **92**, 451 (2008)
38. B. Tuzson, M.J. Zeeman, M.S. Zahniser, L. Emmenegger, *Infrared Phys. Technol.* **51**, 198 (2008)
39. L. Croizé, D. Mondelain, C. Camy-Peyret, M. Delmotte, M. Schmidt, *Rev. Sci. Instrum.* **79**, 043101 (2008)
40. T.J. Griffis, S.D. Sargent, J.M. Baker, X. Lee, B.D. Tanner, J. Greene, E. Swiatek, K. Billmark, *J. Geophys. Res. Atmos.* **113**, D08304 (2008)
41. D. Richter, B.P. Wert, A. Fried, P. Weibring, J.G. Walega, J.W.C. White, B.H. Vaughn, F.K. Tittel, *Opt. Lett.* **34**, 172 (2009)
42. R.Q. Iannone, S. Kassi, H.-J. Jost, M. Chenevier, D. Romanini, H.A.J. Meijer, S. Dhanyala, M. Snels, E.R.T. Kerstel, *Isot. Environ. Health Stud.* **45**, 303 (2009)
43. C. Dyroff, D. Fütterer, A. Zahn, *Appl. Phys. B* **98**, 537 (2010)
44. P. Sturm, A. Knohl, *Atmos. Meas. Tech.* **3**, 67 (2010)
45. L. Wang, K.K. Caylor, D. Dragoni, *Rapid Commun. Mass Spectrom.* **23**, 530 (2009)
46. M.F. Witinski, D.S. Sayres, J.G. Anderson, *Appl. Phys. B* (2010, this issue)
47. H. Waechter, J. Mohn, B. Tuzson, L. Emmenegger, M.W. Sigrist, *Opt. Express* **16**, 9239 (2008)
48. A. Lambrecht, Th. Beyer, M. Braun, A. Peter, S. Hartwig, *Tech. Mess.* **71**, 311 (2004)
49. A. Lambrecht, Th. Beyer, K. Hebestreit, R. Mischler, W. Petrich, *Appl. Spectrosc.* **60**, 729 (2006)
50. A. Fried, B. Henry, B. Wert, S. Sewell, J.R. Drummond, *Appl. Phys. B* **67**, 317 (1998)
51. W.P. Dubé, S.S. Brown, H.D. Osthoff, M.R. Nunley, S.J. Ciciora, M.W. Paris, R.J. McLaughlin, A.R. Ravishankara, *Rev. Sci. Instrum.* **77**, 034101 (2006)
52. C.L. Schiller, H. Bozem, C. Gurk, U. Parchatka, R. Königstedt, G.W. Harris, J. Lelieveld, H. Fischer, *Appl. Phys. B* **92**, 419 (2008)
53. J.B. McManus, J.H. Shorter, D.D. Nelson, M.S. Zahniser, D.E. Glenn, R.M. McGovern, *Appl. Phys. B* **92**, 387 (2008)
54. D.D. Nelson, J.B. McManus, S. Urbanski, S. Herndon, M.S. Zahniser, *Spectrochim. Acta A* **60**, 3325 (2004)
55. L. Joly, C. Robert, B. Parvitte, V. Catoire, G. Durry, G. Richard, B. Nicoullaud, V. Zéninari, *Appl. Opt.* **47**, 1206 (2008)
56. D.A. Brazhnikov, I.V. Nikolaev, V.N. Ochkin, M.V. Spiridonov, S.N. Tskhai, *Laser Phys.* **19**, 1323 (2009)
57. F. D'Amato, M. De Rosa, *Opt. Laser Eng.* **37**, 533 (2002)
58. P. Werle, K. Maurer, R. Kormann, R. Mücke, F. D'Amato, T. Lancia, A. Popov, *Spectrochim. Acta A* **58**, 2361 (2002)
59. R. Wada, J.M. Beames, A.J. Orr-Ewing, *J. Atmos. Chem.* **58**, 69 (2007)
60. A. Fried, S. Sewell, B. Henry, B.P. Wert, T. Gilpin, J.R. Drummond, *J. Geophys. Res. Atmos.* **102**, 6253 (1997)
61. N. Marron, C. Plain, B. Longdoz, D. Epron, *Plant Soil* **318**, 137 (2009)
62. X.T. Lou, G. Somesfalean, Z.G. Zhang, S. Svanberg, *Appl. Phys. B* **94**, 699 (2009)
63. V.L. Kasyutich, R.J. Holdsworth, P.A. Martin, *Appl. Phys. B* **92**, 271 (2009)
64. T. Wu, W. Zhao, W. Chen, W. Zhang, X. Gao, *Appl. Phys. B* **94**, 85 (2009)
65. E.J. Moyer, D.S. Sayres, G.S. Engel, J.M. St. Clair, F.N. Keutsch, N.T. Allen, J.H. Kroll, J.G. Anderson, *Appl. Phys. B* **92**, 467 (2008)
66. R. Kormann, H. Müller, P. Werle, *Atmos. Environ.* **35**, 2533 (2001)
67. P. Werle, R. Kormann, *Appl. Opt.* **40**, 846 (2001)
68. D.R. Bowling, S.D. Sargent, B.D. Tanner, J.R. Ehleringer, *Agric. For. Meteorol.* **118**, 1 (2003)
69. P.S. Kroon, A. Hensen, H.J.J. Jonker, M.S. Zahniser, W.H. van 't Veen, A.T. Vermeulen, *Biogeosciences* **4**, 715 (2007)
70. D.M.D. Hendriks, A.J. Dolman, M.K. van der Molen, J. van Huissteden, *Atmos. Chem. Phys.* **8**, 431 (2008)
71. I. Mammarella, P. Werle, M. Pihlatie, W. Eugster, S. Haapanala, R. Kiese, T. Markkanen, Ü. Rannik, T. Vesala, *Biogeosciences* **7**, 427 (2010)
72. A. Neffel, C. Ammann, C. Fischer, C. Spirig, F. Conen, L. Emmenegger, B. Tuzson, S. Wahlen, *Agric. For. Meteorol.* **150**, 775 (2010)
73. W. Eugster, P. Plüss, *Agric. For. Meteorol.* **150**, 841 (2010)
74. P. Werle, *Agric. For. Meteorol.* **150**, 832 (2010)
75. A. Hyvarinen, J. Karhunen, E. Oja, *Independent Component Analysis*. Series on Adaptive and Learning Systems for Signal Processing, Communications and Control (Wiley-Interscience, New York, 2001)
76. S. Tauber, D. Dean, *J. Soc. Ind. Appl. Math.* **8**, 174 (1960)
77. C.A. Greenhall, *IEEE Trans. Instrum. Meas.* **40**, 994 (1991)
78. S. Mallat, *IEEE Trans. Pattern Anal. Mach. Intell.* **II**, 674 (1989)
79. P. Flandrin, *IEEE Trans. Inf. Theory* **38**, 910 (1992)
80. I. Daubechies, *Ten Lectures on Wavelets*. CBMS-NSF Lecture Notes, vol. 61 (SIAM, Philadelphia, 1992)
81. A. Haar, *Math. Ann.* **69**, 331 (1910)
82. E. Foufoula-Georgiou, P. Kumar, (eds.), *Wavelets in Geophysics*, (Academic Press, San Diego, 1994) pp. 325-344
83. W. Eugster, W. Senn, *Bound.-Layer Meteorol.* **74**, 321-340 (1995)
84. A. Ibrom, E. Dellwik, H. Flyvbjerg, N.O. Jensen, K. Pilegaard, *Agric. For. Meteorol.* **147**, 140 (2007)
85. E. Hecht, *Optics* (Addison-Wesley, Reading, 1998)
86. E. Jennings, *Appl. Opt.* **23**, 1299 (1984)
87. C. Nicolas, A.W. Mantz, *Appl. Opt.* **28**, 4525 (1989)
88. J. Clar, R. Schieder, M. Reich, G. Winnewisser, *Appl. Opt.* **28**, 1648 (1989)
89. P. Werle, *Infrared Phys. Technol.* **37**, 59 (1996)
90. P. Werle, F. Slemr, M. Gehrtz, C. Bräuchle, *Appl. Phys. B* **49**, 99 (1989)
91. P. Werle, F. Slemr, M. Gehrtz, C. Bräuchle, *Appl. Opt.* **28**, 1638 (1989)
92. J. Morville, D. Romanini, A.A. Kachanov, M. Chenevier, *Appl. Phys. B* **78**, 465 (2004)
93. D.T. Cassidy, J. Reid, *Appl. Phys. B* **29**, 279 (1982)
94. J.A. Silver, A.C. Stanton, *Appl. Opt.* **27**, 1914 (1988)
95. F. Persson, M. Andersson, M. Andersson, S. Svanberg, *Appl. Phys. B* **87**, 523 (2007)
96. J.B. McManus, P.L. Keabian, M.S. Zahniser, *Appl. Opt.* **34**, 3336 (1995)
97. J.B. McManus, *Appl. Opt.* **46**, 472 (2007)
98. D.D. Nelson, J.H. Shorter, J.B. McManus, M.S. Zahniser, *Appl. Phys. B* **75**, 343 (2002)

99. C. Webster, *J. Opt. Soc. Am. B* **2**, 1464 (1985)
100. S. Bomse, D.J. Kane, *Appl. Phys. B* **85**, 461 (2006)
101. P. Werle, B. Scheumann, J. Schandl, *Opt. Eng.* **33**, 3093 (1994)
102. H. Riris, C.B. Carlisle, R.E. Warren, D.E. Cooper, *Opt. Lett.* **19**, 15 (1994)
103. P. Werle, *Appl. Phys. B* **60**, 499 (1995)
104. P. Werle, B. Jänker, *Opt. Eng.* **35**, 2051 (1996)
105. G.C. Edwards, G.W. Thurtell, G.E. Kidd, G.M. Dias, C. Wagner-Riddle, *Agric. For. Meteorol.* **115**, 71 (2003)
106. R.B. Stull, *An Introduction to Boundary Layer Meteorology* (Kluwer Academic, Dordrecht, 1988)
107. X.L. Lee, W. Massman, B. Law, *Handbook of Micrometeorology* (Kluwer Academic, Dordrecht, 2004)
108. T. Foken, *Micrometeorology* (Springer, Berlin, 2008)
109. G.I. Taylor, *Proc. R. Soc. Lond., Ser. A* **164**, 476 (1938)
110. A.N. Kolmogorov, *Dokl. Acad. Sci. USSR* **31**, 301 (1941)
111. J.C. Kaimal, J.C. Wyngaard, Y. Izumi, O.R. Cote, Q. J. R. Meteorol. Soc. **98**, 563 (1972)
112. L.F. Burlaga, L.W. Klein, *J. Geophys. Res.* **91**, 347 (1986)
113. S.M. Fan, S.C. Wofsy, P.S. Bakwin, D.L. Jacob, S.M. Anderson, P.L. Keibian, J.B. McManus, C.E. Kolb, D.R. Fitzjerald, *J. Geophys. Res.* **97**, 16627 (1992)
114. S.B. Verma, F.G. Ullman, D. Billesbach, R.J. Clement, J. Kim, E.S. Verry, *Bound.-Layer Meteorol.* **58**, 289 (1992)
115. K.A. Smith, H. Clayton, J.R.M. Arah, S. Christensen, P. Ambus, D. Fowler, K.J. Hargreaves, U. Skiba, G.W. Harris, F.G. Wienhold, L. Klemetsson, B. Galle, *J. Geophys. Res.* **99**, 16541 (1994)
116. F.G. Wienhold, H. Frahm, G.W. Harris, *J. Geophys. Res.* **99**, 16557 (1994)
117. M.S. Zahniser, D.D. Nelson, J.B. McManus, P.L. Keibian, *Philos. Trans. R. Soc. Lond., Ser. A* **351**, 371 (1995)
118. D. Fowler, K.J. Hargreaves, U. Skiba, R. Milne, M.S. Zahniser, J.B. Moncrieff, I.J. Beverland, M.W. Gallagher, *Philos. Trans. R. Soc. Lond. A* **351**, 339 (1995)
119. D.C. Hovde, T.P. Meyers, A.C. Stanton, D.R. Matt, *J. Atmos. Chem.* **20**, 141 (1995)
120. M. Pihlatie, J. Rinne, P. Ambus, K. Pilegaard, J.R. Dorsey, Ü. Rannik, T. Markkanen, S. Launiainen, T. Vesala, *Biogeosciences* **2**, 377 (2005)
121. E. Pattey, I.B. Strachan, R.L. Desjardins, G.C. Edwards, D. Dowa, J.I. MacPherson, *Agric. For. Meteorol.* **136**, 222 (2006)
122. J. Rinne, T. Riutta, M. Pihlatie, M. Aurela, S. Haapanala, J.P. Tuovinen, E.-S. Tuittila, T. Vesala, *Tellus B* **59**, 449 (2007)
123. C. Wille, L. Kutzbach, T. Sachs, D. Wagner, E.M. Pfeiffer, *Glob. Change Biol.* **14**, 1395 (2008)
124. D. Zona, W.C. Oechel, J. Kochendorfer, K.T. Paw U, A.N. Salyuk, P.C. Olivas, S.F. Oberbauer, D.A. Lipson, *Glob. Biogeochem. Cycles* **23**, GB2013 (2009)
125. D.R. Bowling, J.B. Miller, M.E. Rhodes, S.P. Burns, R.K. Monson, D. Baer, *Biogeosciences* **6**, 1311 (2009)
126. E.R. Crosson, *Appl. Phys. B* **92**, 403 (2008)
127. D. Famulari, E. Nemitz, C. Di Marco, G.J. Phillips, R. Thomas, E. House, D. Fowler, *Agric. For. Meteorol.* **150**, 786 (2010)
128. W. Gao, R.H. Shaw, K.T. Paw U, *Bound.-Layer Meteorol.* **47**, 349 (1989)
129. C. Thomas, T. Foken, *Appl. Climatol.* **80**, 91 (2005)
130. J.F. Howell, L. Mahrt, *Bound.-Layer Meteorol.* **83**, 117 (1997)